Phys. Status Solidi A **206**, No. 1, 21–30 (2009) / **DOI** 10.1002/pssa.200824257

physica status solidi a
www.pss-a.com
applications and materials science

Stability of dislocation structures in copper towards stress relaxation investigated by high angular resolution 3D X-ray diffraction

Bo Jakobsen[1,2], Henning Friis Poulsen[1], Ulrich Lienert[3], Joel Bernier[3,4], Carsten Gundlach[1,5], and Wolfgang Pantleon[*,1]

[1] Center for Fundamental Research: Metal Structures in Four Dimensions, Materials Research Department, Risø National Laboratory for Sustainable Energy, Technical University of Denmark, Frederiksborgvej 399, 4000 Roskilde, Denmark
[2] Center for Fundamental Research: Glass and Time, Department of Science, Systems and Models, Roskilde University, Universitetsvej 1, 4000 Roskilde, Denmark
[3] Argonne National Laboratory, APS, 9700 South Cass Ave., Argonne, IL 60439, USA
[4] Engineering Technologies Division, Lawrence Livermore National Laboratory, 7000 East Avenue, Livermore, CA 94551, USA
[5] European Synchrotron Research Facility, 6 rue Jules Horowitz, 38043 Grenoble Cedex, France

Received 24 June 2008, revised 13 August 2008, accepted 20 August 2008
Published online 25 September 2008

PACS 61.05.cp, 61.72.Lk, 62.20.F–, 62.40.+i, 81.70.Bt

[*] Corresponding author: e-mail wolfgang.pantleon@risoe.dk, Phone: +45 4677 5791, Fax: +45 4677 5758

A 300 µm thick tensile specimen of OFHC copper is subjected to a tensile loading sequence and deformed to a maximal strain of 3.11%. Using the novel three-dimensional X-ray diffraction method 'High angular resolution 3DXRD', the evolution of the microstructure within a deeply embedded grain is characterised *in-situ* by the behaviour of individual subgrains. The loading sequence consists of three continuous deformation stages with strain rates of 1.1×10^{-6} s^{-1} and 3×10^{-2} s^{-1}, in each case followed by a period of extended stress relaxation at fixed motor positions, as well as an unloading step. In contrast to the deformation stages, during each stress relaxation stage, number, size and orientation of subgrains are found to be constant, while a minor amount of clean-up of the microstructure is observed as narrowing of the radial X-ray diffraction line profile. The associated decrease in the width of the strain distribution indicates homogenization of the elastic strains present in the deformation structure. During reloading, the subgrain structure seemingly starts to develop further when the entire dislocation structure is deforming plastically. Upon unloading of the sample, the average backward strain of the subgrains increases.

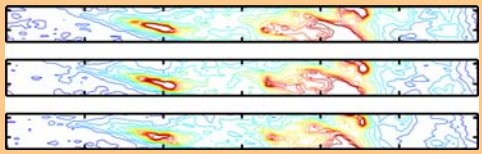

Projections of reciprocal space maps obtained just before (top) and after (middle) stopping the traction and after half an hour of stress relaxation (bottom). No major changes in the microstructure occur, only minor adjustments are observed.

1 Introduction Understanding the dynamics of dislocation structures is a key problem for modelling crystal plasticity. A generally accepted theoretical framework is lacking, as a number of basic questions are still unsettled, such as the nature of the formation of ordered dislocation structures, their evolution (by continued subdivision) and their stability.

Part of the problem has been the lack of suitable techniques for characterising structural dynamics. Transmission electron microscopy provides very comprehensive static information, but such studies are intrinsically restricted to thin foils and hence even *in-situ* studies will in general not be representative of bulk dynamics (see e.g. [1–3]). On the other hand, X-ray diffraction techniques

such as line profile and rocking curve analysis (e.g. [4–7]) can probe bulk dynamics, but the results are highly indirect as they represent averages over many subgrains or grains with different sizes, orientations and neighbouring environments. Hence models are required for an interpretation of the data; the use of which introduces assumptions which are often hard to verify by independent measurements.

Recently two synchrotron based methods have been developed that enable three dimensional characterisation on the micrometer scale: three-dimensional X-ray diffraction (3DXRD) microscopy [8, 9] and 3D X-ray crystal microscopy [10]. However, at present both methods have limitations: the spatial and angular resolution of the 3DXRD microscope does not allow for direct observation of the deformation microstructure, whereas the spatial scanning technique of the 3D X-ray crystal microscope makes data acquisition slow – far from ideal for time-resolved studies.

To overcome these issues, we have developed an *in-situ* characterisation technique 'High angular resolution 3DXRD' [11, 12]. This method enables acquisition of 3D reciprocal space maps with high resolution (of the order of 1×10^{-3} Å^{-1}). From such maps, quantitative information can be obtained on size, orientation, mean elastic strain, and internal elastic strain distribution of a set of individual subgrains, all deeply embedded within a thick polycrystalline specimen. Moreover, a reasonable time resolution of the order of minutes has been achieved for mapping of an entire grain. In a first study of the microstructural evolution in a bulk, a copper tensile specimen was loaded incrementally from 3% to 4.2% elongation and characterised at each load increment. The observed evolution of the subgrains is contrary to conventional expectations and has lead to the suggestion that the dislocation structure follows an intermittent dynamics [11].

In the present work, we have improved the instrumental design, such that the microstructure evolution can be studied during continuous deformation. This enables us to address longstanding issues related to the response of the subgrain structure to continuous deformation, strain relaxation and unloading.

2 Experimental

2.1 Sample The sample material is 99.99% pure OFHC polycrystalline copper. It was initially cold-rolled to a reduction of 80% with a resulting thickness of 300 µm and then fully recrystallized by annealing for 120 minutes at 450 °C. With electron backscatter diffraction the average grain size (ignoring twin boundaries) is determined to about 30 µm. Dog bone shaped tensile samples with a gauge length of 8 mm and a gauge width of 3 mm are prepared by spark cutting. The investigation reported here is performed at room temperature on a single specimen.

2.2 3DXRD experiment The experiment is performed at the X-ray Operations and Research beamline 1-ID at the Advanced Photon Source (Argonne National Laboratory, USA). The X-ray beam is delivered by a combination of optical elements comprising a 6-bounce monochromator and vertical focusing by refractive lenses (for details see [11]). The 52 keV X-ray beam has a vertical divergence of 17 µrad and a relative energy spread of 7×10^{-5}. The beam size is defined by slits to be 30 µm horizontally and 20 µm vertically.

The sample is placed in a custom made load frame which is positioned on translation stages mounted on a Huber 3-axes Eulerian cradle. The load frame is screw driven and operated in position-control via the screw driving motor. The macroscopic strain in the gauge section of the specimen is measured by a single surface-mounted linear strain gauge coupled to a Wheatstone bridge. The macroscopic stress is determined by a load cell integrated in the load frame.

Initially diffraction patterns are recorded in the undeformed state using a conventional CCD area detector positioned at a distance of 253 mm behind the sample. By use of 3DXRD principles (e.g. [9]) a bulk grain is identified. The selected grain has a 400 reciprocal lattice vector aligned within 9° of the tensile direction. The grain is scanned through the beam and found to have dimensions of 15 µm and 13 µm in horizontal and vertical direction, respectively. Next, the specimen is rotated such that the respective 400 reflection is observable in the vertical diffraction plane. The geometry of the setup is sketched in Fig. 1.

For the high resolution mapping, a MarCCD 165 area detector is used in 1024×1024 pixel mode, exhibiting a 161×161 µm pixel size. This detector is positioned at a horizontal distance L of 3737 mm behind the sample and on the vertical diffraction plane such that the selected 400 reflection is centred on the detector. Data acquisition consists of rocking the sample in equidistant steps of $\Delta\omega = 0.005°$ around the horizontal ω-axis, perpendicular to the direction of the incoming beam. Continuous sampling is achieved by rocking the sample (rotating with constant speed) through the interval $\Delta\omega$ during each exposure. The exposure time is 10 seconds.

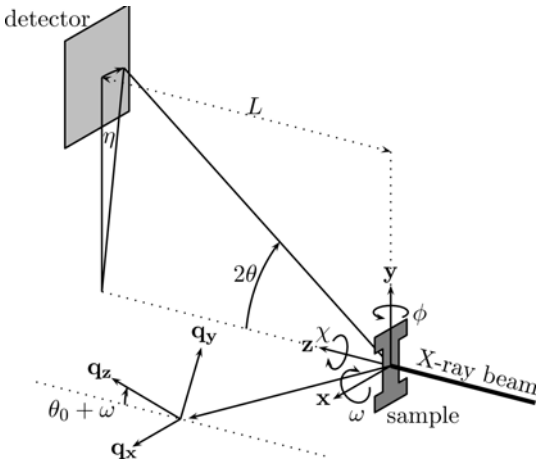

Figure 1 Sketch of the diffraction geometry and the reciprocal space coordinate system used (from [12]).

3D reciprocal space maps of the 400 reflection are generated from such sets of consecutive ω-intervals (as described in detail in [11, 12]). The maps are parameterised by (q_x, q_y, q_z), with q_x parallel to the horizontal axis of the detector, q_y the radial direction (i.e. parallel to the scattering vector) and q_z perpendicular to q_x and q_y (see Fig. 1).

In this manner, variations in q_y indicate elastic lattice strains

$$\varepsilon = \frac{q_{y,0} - q_y}{q_y}, \tag{1}$$

whereas differences in q_x and q_z represent orientation variations. The instrumental resolution in q_x and q_y are both 0.001 Å^{-1} – predominantly limited by detector resolution – while the resolution in q_z is 0.0006 Å^{-1}, as determined by the step size $\Delta\omega$.

During the experiment, reciprocal space maps are acquired repeatedly. The maps are truncated in q_z by limiting the number of ω-intervals to 15, thereby improving the time resolution to 3.6 min. To provide a better overview, at selected time steps larger ω-ranges are gathered. During loading the load frame is translated parallel to the load axis to compensate the sample elongation, such that the beam at all times fully illuminates the selected grain. To estimate the accuracy of this position correction procedure, and check for drifts in general, at selected times the grain is scanned with respect to the beam. From these tests it is estimated that the positional fluctuations are at most 2 µm. Given the size of the grain and the beam, this implies that all parts of the grain are completely illuminated during all acquisition intervals.

2.3 Loading sequence The sequence is illustrated in Fig. 2 by the displacement of the cross-head driving tension motor as function of time and the resulting stress–strain curve obtained from the strain gauges and the load cell. The loading sequence comprises the following steps:

Preloading The sample is preloaded in small steps to a tensile strain of 1.82% (i.e. the macroscopic strain monitored by the strain gauge). By following the movement of the grain during this straining, a calibration curve is produced relating the displacement of the tension motor to the resulting macroscopic strain and the spatial grain movement.

First slow loading and hold The sample is strained continuously with a strain rate of 1.1×10^{-6} s^{-1} to a tensile strain of 2.315%. During the slow loading 20 reciprocal space maps are gathered. After that, the tension motor is stopped and the sample held at constant position of the tension motor for 41 hours, during which the tensile strain increases to 2.365%. During the first hour another 19 reciprocal space maps are gathered. Unfortunately, for the remainder of the time diffraction data are unavailable due to a synchrotron break-down. Due to unavoidable drifts of the monochromator, a direct comparison of data obtained before and after the long break is questionable and not performed here.

Second slow loading and hold After re-centring of the grain with respect to the beam, the sample is strained continuously with the same strain rate of 1.1×10^{-6} s^{-1} to a tensile strain of 2.682%. During this period 14 reciprocal space maps are gathered. The sample is then held at constant motor position for 2.2 hours, while gathering 10 maps during the first 45 minutes. At the end of the hold, the strain has increased to 2.695%.

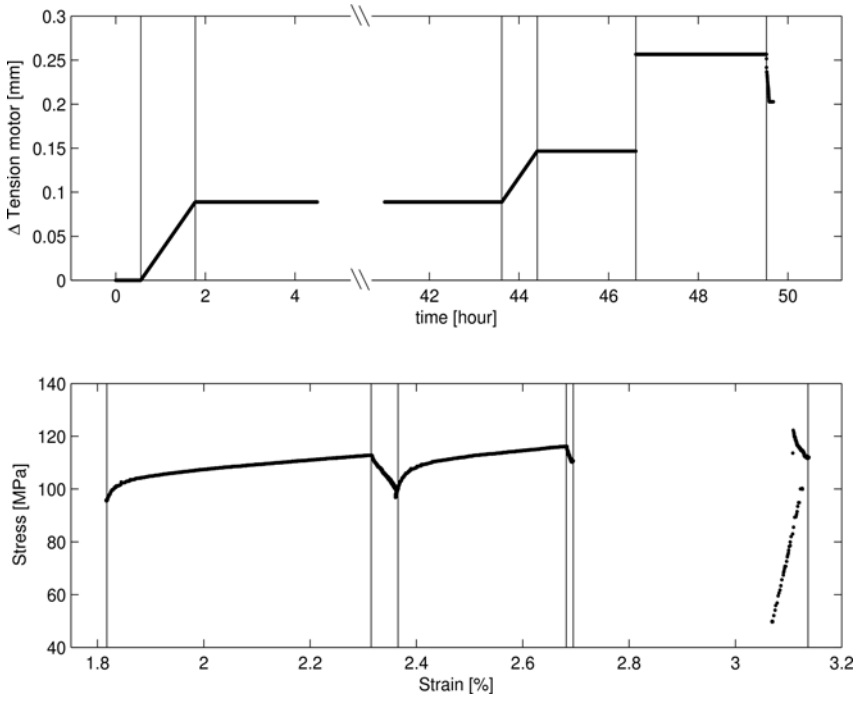

Figure 2 Loading sequence. (top) Displacement of tension motor versus time, (bottom) stress–strain curve determined from load cell and strain gauge. Vertical lines separate the different stages of the sequence. The rate of the last loading is too fast to collect stress and strain data during the loading.

Fast loading and hold Next, the sample is strained to 3.110% as fast as possible with the present setup. The estimated strain rate is 3×10^{-2} s^{-1}. Following this, the sample is held at constant tension motor displacement for 2.9 h, after which the tensile strain of the specimen has increased to 3.137%. A total of 12 reciprocal space maps are gathered. The acquisition of the first map is started within one second after stopping the loading. The 10 first maps are taken continuously during the first 35 minutes after fast straining. The last two are taken after a total time of 53 and 131 minutes after straining, respectively.

Unloading Finally, the sample is unloaded during 221 seconds from a macroscopic stress of 111.9 MPa to 49.7 MPa. Rather large reciprocal space maps (comprising 60 ω-intervals) are acquired before and after unloading.

3 Results

3.1 Mechanical behaviour As obvious from the stress–strain curve in Fig. 2 the flow stress increases during the loading stages and the material work-hardens. (The values for the flow stress are in agreement with tensile tests on OFHC copper of comparable grain size at room temperature and similar strain rate [13].)

When the motion of the tension motor is stopped, the gauge section of the specimen continues to deform plastically in tension due to the applied tensile load (cf. [14, 15]). As the total length of specimen and mounting gear is fixed, an extension of the gauge section of the specimen must be compensated by elastic unloading of other parts of the specimen and the mounting gear. Any plastic straining in the specimen leads to a lowering of the elastic strains in the system accompanied by a reduction of the applied stresses. In this manner, the applied stress is relaxed despite the fixed total elongation.

During stress relaxation under fixed motor displacements, the stress decreases linearly with the total strain $\Delta\varepsilon$ in the gauge section of the specimen (e.g. [14, 15])

$$\Delta\sigma = \sigma - \sigma_0 = -E_{\mathrm{m}}\,\Delta\varepsilon\,, \tag{2}$$

from the value σ_0 when stopping the tension motor (a similar relation holds for the plastic strain in the gauge section; only the applicable, effective machine modulus E_{m} will be different). Such a linear dependence is nicely seen in the stress–strain curve in Fig. 2 for the extended first holding stage from 2.315% to 2.365%.

Stress relaxation at constant temperature T is commonly described (e.g. [14–16]) by a logarithmic time dependence of the stress drop

$$\Delta\sigma = -\frac{kT}{V}\ln\left(1+\frac{t}{\tau}\right), \tag{3}$$

with Boltzmann constant k, a characteristic relaxation time τ and an apparent activation volume V. Such a logarithmic dependence can be derived from quite general considerations [17, 18]; more elaborate analytical expressions proposed as well (cf. [14, 19]) will not be considered here.

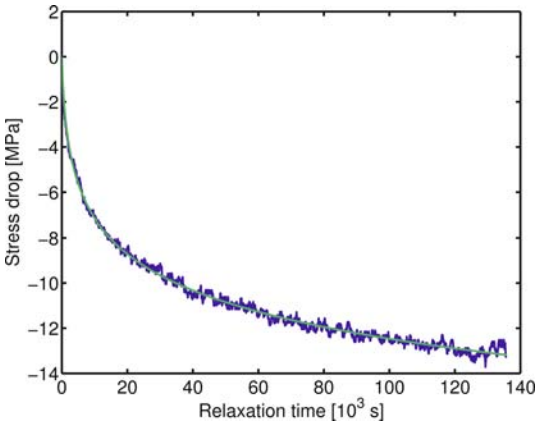

Figure 3 (online colour at: www.pss-a.com) Stress relaxation during first holding stage. A logarithmic decrease of the stress is fitted to the experimental data.

As shown in Fig. 3 a logarithmic dependence with $\tau = 510$ s and $V = 100b^3$ (with Burgers vector $\boldsymbol{b} = 0.256$ nm) describes the experimental data accurately during 37 h. Both activation parameters are not constant during relaxation; in particular the data from the first 20 min are better described by a shorter relaxation time (150 s) and a larger activation volume ($150b^3$).

In the second tensile loading stage with the same strain rate as in the first one, plastic flow is observed for stresses above the initial yield stress, but before the maximal flow stress of the first loading stage is reached. The work-hardening rate is slightly higher in the second loading stage than in the first.

3.2 Reciprocal space maps The main results of the experiment are the gathered reciprocal space maps which can be combined into a three-dimensional movie. Here selected snapshots from the time series are presented where for each point in time the three-dimensional reciprocal space is projected onto a two-dimensional subspace. Two projections are used: one onto the (q_x, q_z)-plane (i.e. the azimuthal plane) and one onto the (q_x, q_y)-plane (similar to the raw detector images, slightly corrected for distortion). The first projection corresponds to integrating over the elastic strain degree of freedom and visualising the mosaic spread – in other words a zoom on a small part of the 400 pole figure for the selected grain. The second projection represents integration over the mosaic spread in the direction of the truncated q-range (rocking direction) and enables a convenient visualisation of the evolution of lattice strains.

As an example, Fig. 4 provides a tableau of both types of projections for part of the initial loading from 1.817% to 2.010%. Evidently, the reciprocal space map is characterised by a set of sharp peaks on top of a diffuse cloud of enhanced intensity. Distinct peaks in such a map originate from single and nearly dislocation free subgrains in the grain of interest [11, 20]. More extended islands like the one to the left in the images in the left column of Fig. 4 are likely to be compound peaks, comprising contributions

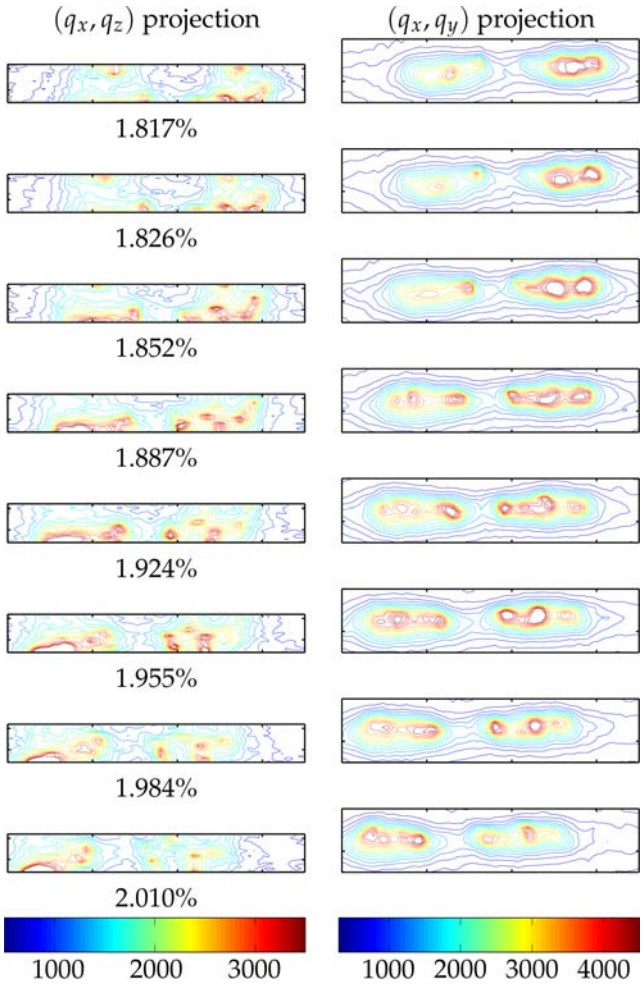

Figure 4 (online colour at: www.pss-a.com) Projections of eight 3D reciprocal space maps obtained during the first loading. The projections each cover the same range [–0.04 Å^{-1}, 0.03 Å^{-1}], [6.925 Å^{-1}, 6.490 Å^{-1}], and [0.027 Å^{-1}, 0.036 Å^{-1}] in q_x, q_y, and q_z, respectively. They are plotted with axis of equal scale. The maps shown are truncated in q_x direction with respect to the full dataset. The colour bar is in arbitrary units of integrated intensity.

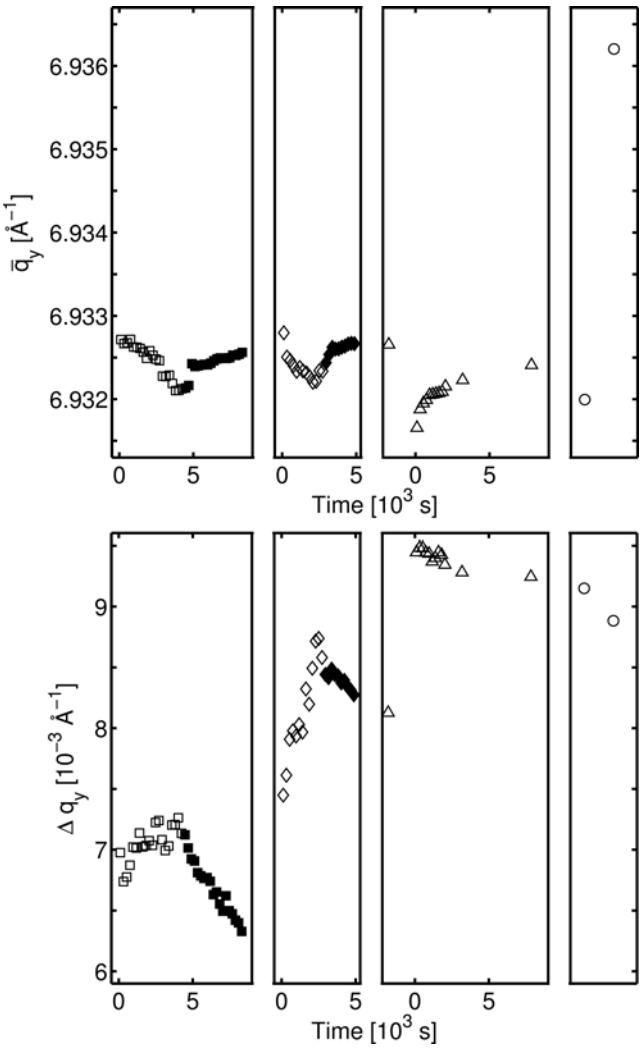

Figure 5 Average value ($\bar{q}_y$) and width (Δq_y) of the radial peak profiles (i.e. azimuthally integrated peak profiles) as function of time. The time in each part is measured with respect to the start of the deformation. First slow loading (open square) and holding (filled square), second slow loading (open diamond) and holding (filled diamond), holding after fast loading (triangles pointing up), and unloading (circles). Note that the first point for the fast loading is even before the loading starts, hence at a negative time.

from several subgrains. The diffuse cloud is interpreted as arising from the disordered boundary regions of high dislocation density (dense dislocation walls) between the subgrains [11, 21].

Comprehensive information on a particular subgrain can be derived from each distinct peak [12]. More specifically, the integrated intensity of a sharp peak is directly proportional to the volume of the subgrain, while the centre-of-mass-position of the peak in reciprocal space ((q_x, q_z) and q_y) relates to average orientation and average lattice strain (along the scattering vector) of the subgrain, respectively. From the peak shape the dislocation density inside the subgrain can be inferred and is found to be rather small [12].

Based on this interpretation the time evolution of the peaks in Fig. 4 can be rationalized in terms of rotation, straining and growth or shrinkage of subgrains. While the information is incomplete in the sense that not all subgrains in the grain are probed (as they give rise to peaks outside the window of observation in q_z) and contributions from some of the subgrains cannot be separated, this type of data is very useful towards addressing whether the geometry of the subgrains and their elastic strain state changes or not. The instrumental resolution in the azimuthal directions (q_x, q_z) corresponds to rotations of 0.008° and 0.005° respectively. The instrumental resolution in the radial direction (q_y) corresponds to a strain resolution of 1.4×10^{-4}. Shifts of the peaks are detectable down to (and even beyond) this limit.

Additional insight is gained from traditional line profiles, i.e. one-dimensional profiles, where the reciprocal space map is integrated over both azimuthal directions (q_x

and q_z). From such radial peak profiles two quantities of interest can be derived (e.g. [7]): the average elastic strain (along the diffraction vector) with respect to the initial unloaded state, and the width of the strain distribution. These are determined from fitting a pseudo Voigt function to the radial peak profile as its centre (identical to the average) and its full width at half of the maximum intensity (FWHM). Both quantities are plotted in Fig. 5 as function of time – covering the complete loading sequence.

A closer inspection of the radial peak profile reveals a slower decay of the intensities at higher q_y values than for smaller q_y. If split pseudo Voigt functions are used to quantify the asymmetry of the radial peak profiles, fitting resolves a larger width at half of the maximum intensity for the tails at higher q_y. The relative asymmetry increases slightly during stress relaxation and more strongly upon unloading.

In the following, the individual stages of the loading sequence are discussed. Selected azimuthal distributions in the (q_x, q_z) plane for the individual stages are presented in Figs. 4 and 6 to 8.

3.3 First and second slow loading During the first loading stage significant changes in the subgrain structure are observable in the reciprocal space maps. In Fig. 4 showing only part of the entire first loading stage the temporary formation of new subgrains and the disappearance of others can be recognized. During the entire tensile loading subgrains of different orientations and elastic strains appear and disappear intermittently (confirming earlier observations [11]). Similar observations are made in the second loading stage.

3.4 Holds after first and second slow loading The results during the two holding stages are quite similar to each other. In both cases, there is no evidence from visual comparison of the reciprocal space maps (cf. azimuthal projections of the second holding stage in Fig. 6) for any microstructural changes on the subgrain level within the approximately first hour of data taking after stopping the tension motor. Extrapolation of the evolution during holding to times prior to the moment of stopping and comparison with the last reciprocal space map during loading even rules out any hypothetical structural changes at the subgrain level, which may occur at the exact time of the stop and are completed before the first measurement of the scan.

From the information of the radial peak profiles summarized in Fig. 5 it is found that during the loading stages the mean position of the radial profile decreases and hence (according to Eq. (1)) the average elastic strain in the illuminated grain increases with increasing stress. During the holding period the elastic strains are decreasing due to stress relaxation. The relaxation of the elastic strain seemingly comprises two components (in particular after the first loading), a fast initial transient, followed by a much slower response.

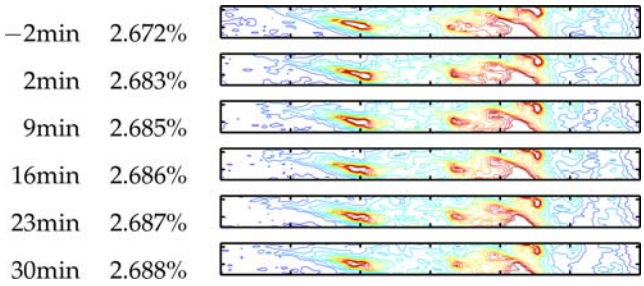

Figure 6 (online colour at: www.pss-a.com) Azimuthal projection of every second of the 10 reciprocal space maps obtained during the second holding, and of the last map obtained while still straining. Time is with respect to the moment where the tension motor is stopped, and for the centre image of each dataset. The projections each cover [0 Å^{-1}, 0.12 Å^{-1}] and [0.027 Å^{-1}, 0.036 Å^{-1}] in q_x and q_z, respectively. The colour bar is as in Fig. 4.

Correspondingly, the width of the internal strain distribution (as observed from the width of the radial profiles) increases during tensile loading, and decreases almost linearly with time during the first hour after stopping the tension motor.

3.5 Fast loading and hold Similarly to the holding stages after the slow loadings, from visual inspection of the reciprocal space maps (including the azimuthal projections in Fig. 7) there is no evidence of any structural evolution at the scale of subgrains upon stopping the tensile motor after fast loading. Likewise, the relaxation of the average elastic strain (as seen from the mean position of the radial profile in Fig. 5) initially occurs fast and slows down later. The width of the mean strain distribution decreases with time after interrupting the tensile motion (initially linearly, but with a reduced rate at later times).

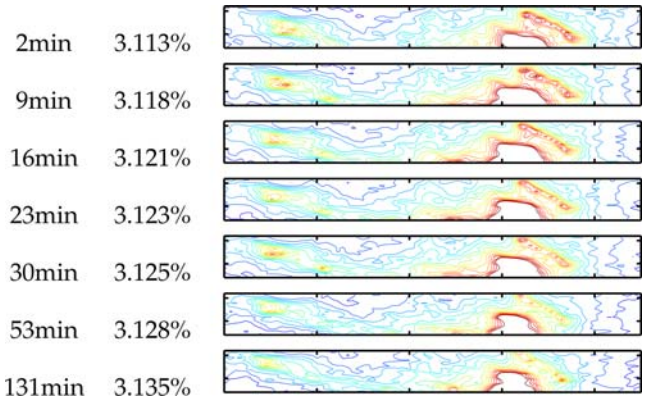

Figure 7 (online colour at: www.pss-a.com) Azimuthal projection of every second of the 10 reciprocal space maps obtained right after the fast loading, and of the two obtained at later times. Time is with respect to the moment where the tensile motor is stopped, and for the centre image of each dataset. The projections each cover [0.02 Å^{-1}, 0.11 Å^{-1}], and [0.027 Å^{-1}, 0.036 Å^{-1}] in q_x and q_z, respectively. The colour bar is as in Fig. 4.

As no observations of the microstructure are available during the fast loading stage, a structural relaxation could have taken place in the time interval between holding and taking of first data. By noting that the data from the first ω-interval in the first reciprocal space map obtained after stopping the tension motor are identical to the data of the same interval in consecutive maps, it is concluded that such hypothetical rearrangements would have to have relax completely within the first 5 seconds after the hold.

3.6 Unloading By inspection it is found that the two reciprocal space maps obtained just prior to and after unloading (with azimuthal projections shown in Fig. 8) are nearly identical but shifted with respect to each other in reciprocal space. Seven individual well separated peaks are identified and analyzed in detail. Three independent pseudo Voigt functions are fitted to each peak, one in each of the three reciprocal space directions, giving the position of the maximum of the peak (the single peak analysis technique is described in detail in [12]).

Based on these seven peaks it is found that the two maps in Fig. 8 on average are shifted with respect to each other by –0.0072 Å^{-1}, and –0.0034 Å^{-1} in q_x, and q_z, respectively. Such an overall offset is readily explained by a rotation of the whole sample or a rotation of the entire grain driven by the compatibility with neighbouring grains during unloading. However, small differences between the shifts of individual subgrains are observed. The standard deviations for the subgrain shifts in both azimuthal directions are 13% and 20% of the overall offset in q_x, and q_z, respectively. These differences between the rotations of individual subgrains indicate heterogeneity of the elastic unloading within the grain either caused by its neighbours or due to the formation of domains of slightly different orientation within a grain during tensile loading.

The radial (q_y) position of an individual peak represents the mean elastic strain along the scattering vector of the corresponding subgrain. For the identified seven subgrains the elastic strain of each subgrain is less than the mean elastic strain of the grain (determined from $\bar{q}_y$ by

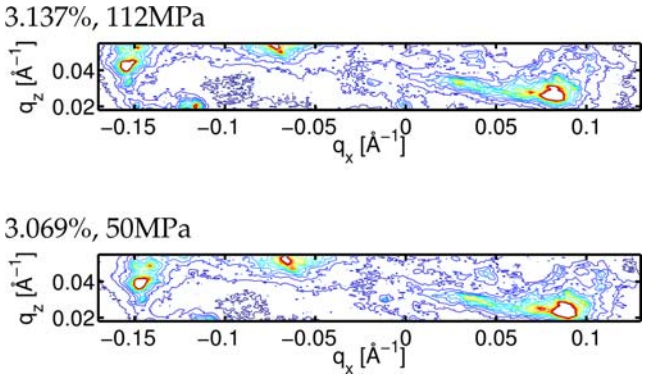

Figure 8 (online colour at: www.pss-a.com) Azimuthal projections of reciprocal space maps obtained before and after unloading the sample. The colour bar is as in Fig. 4.

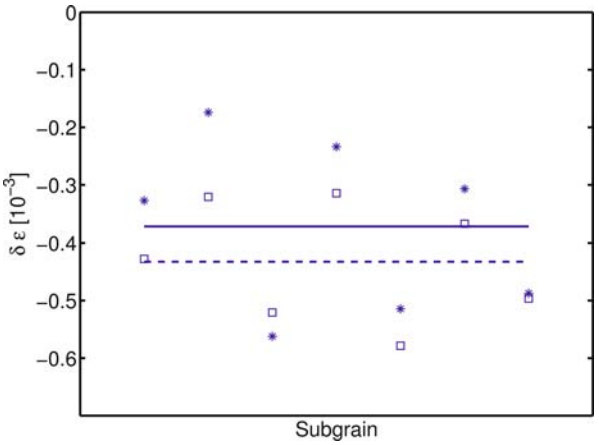

Figure 9 (online colour at: www.pss-a.com) Backward strains (compressive stresses with respect to the grain average) of seven selected subgrains before (stars) and after (squares) unloading of the sample. Their average value is indicated by the full and dashed lines for the loaded and unloaded state, respectively.

Eq. (1)). With respect to the grain average a compressive strain

$$\delta\varepsilon = -\frac{q_y - \bar{q}_y}{q_y} < 0\,, \tag{4}$$

(called backwards strain) is present in each subgrain as illustrated in Fig. 9. The differences between the elastic strains of the seven individual subgrains are rather substantial (but due to the small number of subgrains, their variance shall not be analysed further). Both findings are consistent with the observations on the larger set of subgrains reported in [12].

On unloading the maximum of the integrated radial peak profile shifts to a higher absolute q_y value (see Fig. 5). The shift corresponds to a decrease in the mean tensile elastic strain of the grain of 0.059%. This is comparable to the macroscopic strain difference of 0.067% detected by the strain gauges during unloading (and the differences can be explained at least partially by the angle between the tensile axis and the 400 direction). The width of the radial peak profile decreases by 3% corresponding to a narrowing of the internal strain distribution by the same amount. On the other hand, the compressive strains (with respect to the grain average) of the seven identified subgrains increase during unloading as seen in Fig. 9 – in average by 14% from –0.037% to –0.043%.

4 Discussion

4.1 General All observations are consistent with the following interpretation:

The microstructure – as described in terms of the number of subgrains, their orientation and extension in reciprocal space – develops markedly and in an intermittent manner during continuous loading, but becomes frozen at the instant of interrupting the traction. Within the observation time, individual dislocations are able to migrate under the

applied load further in forward direction. Their motion causes additional plastic deformation of the gauge section of the specimen and hence a specimen elongation. Consequently, the fixed displacement of the motor position requires less elastic deformation (of all parts) and the average elastic strain decreases.

The logarithmic time dependence of the stress relaxation with an apparent activation volume of the order of $100b^3$ is consistent with a thermal activated motion of individual dislocations surmounting obstacles. The nature of the obstacles or a single rate limiting process (jog dragging, cross slip, cutting of forest dislocations) cannot be deduced from the data. Several different stress relaxation tests at different temperatures would have to be analysed [15].

Comparable values for the apparent activation volume during stress relaxation have been reported for OFHC copper [14], but significantly larges values have been obtained on pure copper as well [16, 22] depending on both the applied stress and the used equipment; a proper assessment of the later effect requires thorough determination of the machine stiffness (cf. [22]).

Dislocations having moved along a certain path may find an annihilation partner and annihilate. Hence, the forward motion of some dislocations is accompanied by a reduction of the dislocation density and both effects cause a narrowing of the elastic strain distribution. The observed decrease in the width of the radial peak profile is a consequence of such a cleaning-up of the dislocation structure.

A similarly frozen subgrain structure persists during unloading again accompanied by a certain amount of cleaning-up evidenced by a reduction in the width of the radial peak profile. In this case, however, piled-up dislocations may move backwards, dislocation loops shrink and disappear reducing the total dislocation density. Differences in rotations and elastic straining between individual subgrains indicate locally heterogeneous changes in the elastic stress states of the individual subgrains during unloading.

Interestingly the changes occurring during unloading are less prominent than the changes during stress relaxation (in particular during the first hour of the first holding stage, cf. Fig. 5). This is due to the still applied stress and the ongoing thermally activated plastic deformation in forward direction under stress relaxation, whereas unloading allows only moving back of individual mobile dislocations which have been hindered in their forward motion by obstacles and stored only dynamically under the applied load.

4.2 Relation to composite model The backward strains of individual subgrains (compressive strains compared to the grain average) can be rationalized in terms of a modified composite model. Analogous to the original composite model [23, 24] for an inhomogeneous deformation structure, compatibility of deformation requires larger local stresses for the dislocation-dense boundaries (as higher dislocation density causes a larger flow stress) than for the dislocation-depleted regions. The former develop forward stresses, whereas the nearly dislocation-free subgrains experience backward stresses. The amount of backward stress and strain in each individual subgrains, however, is different from subgrain to subgrain – as discussed in [11, 12] and shown in Fig. 9.

During stress relaxation and the associated plastic deformation caused by a forward motion of dislocations, the decreasing width of the radial profile indicates a decrease in the variations of the elastic strains within the grain and hence a lower total dislocation density. The simultaneous increase in asymmetry might be achieved by a sharpening of the strain distribution between the subgrains leading to a more even strain level of the individual subgrains.

Upon unloading the average backward strain of the seven individual subgrains increases, explaining instantly the observed increase in the peak asymmetry. A more detailed quantification of the changes in the distribution of the backward strains of the subgrains requires data on a larger number of subgrains and is in preparation.

4.3 Reloading and forward Bauschinger effect During the 41 hour long holding period following the first loading stage the stress is relaxed significantly, before the specimen is reloaded during the second loading period. For instance, the radial peak width dropped below the value at the beginning of the first loading stage. The reloading behaviour is investigated in more detail for the clearly separable peak observed at the left in the top frame of Fig. 6. The peak is found to rotate with respect to the right part of the map during the second deformation stage.

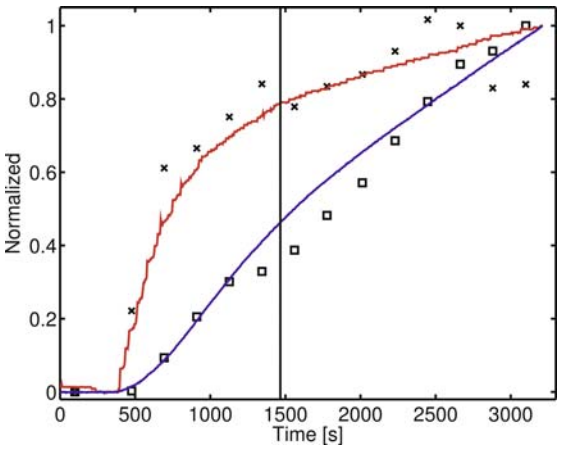

Figure 10 (online colour at: www.pss-a.com) Second loading stage: analysis of the correlation between macroscopic stress (red line) and strain (blue line) in the gauge section of specimen, mean elastic strain (crosses) of the selected grain, and orientation of the selected subgrain in q_x direction (squares). The curves are scaled to obtain maximum correspondence at beginning and end. The vertical line indicates the point where the macroscopic stress reaches the previous maximum flow stress (at the end) of the first loading stage.

In Fig. 10 different information gathered during the entire reloading stage is summarized: the macroscopic stress and strain are plotted together with the mean elastic strain of the grain (obtained from the mean q_y value of the radial peak profile integrated azimuthally over all relevant reciprocal space maps), as well as the azimuthal position (represented by q_x) of the particular peak. All curves are scaled to coincide at start and end of the deformation stage.

Following the constant speed of the tension motor, the macroscopic strain and stress of the gauge section of the specimen both increase with time; the macroscopic strain almost linearly during the entire deformation.

The macroscopic stress increases only at the beginning linearly with time indicating pure elastic behaviour; at a certain instant in time yielding occurs, even before the applied flow stress reaches the maximal flow stress of the first loading stage. In this manner, a forward Bauschinger effect is caused by stress relaxation due to the cleaning-up of the dislocation structure and the reduction of the dislocation density. After yielding, deformation proceeds with a continuously decreasing work-hardening rate.

The mean elastic strain of the grain follows nicely the applied macroscopic stress during the entire deformation stage – as expected from elasticity.

On the other hand, the rotation of the individual peak (represented by q_x) increases initially linearly with time and proportional to the total macroscopic strain. Their proportionality is not restricted to the elastic regime; a clear deviation from linearity is observed first after the material has started to deform plastically, but before the applied stress reaches the previous maximum flow stress. The observation that the onset of a deviation in the rotation from a linear dependence on the macroscopic strain is delayed with respect to the onset of plastic yielding under reloading can be rationalized in terms of the modified composite model: During reloading (after stress relaxation) initially only the dislocation-free subgrains deform plastically (or at least some of them). In this micro-yielding regime, the relation between strain and rotation still holds. Only when yielding of the harder dislocation-rich boundaries occurs as well and the entire dislocation structure deforms plastically, the lattice rotation of an individual subgrain becomes independent of the macroscopic strain and will be controlled by the particular behaviour of its adjacent boundaries.

5 Conclusion The experimental data are all consistent with the notion that the evolution of the microstructure is driven by plastic deformation of the entire dislocation structure:

– The subgrain structure develops continuously and intermittently during tensile testing.

– When the traction is terminated and the tension motor position fixed, the deformation structure freezes, and a clean-up process gives rise to stress relaxation.

– The subgrain structure is unchanged when unloading the sample, but the compressive strains of the subgrains (with respect to the average of the grain) increase in average during unloading.

The results for the prolonged holding periods in this study demonstrate the long-term stability of the high angular resolution 3DXRD method. Thereby they serve as an extra validation of the previous studies [11, 12]. The present findings also add additional insight to the reported intermittent dynamics [11]. One could have speculated that the observed intermittence is a signature of quite unstable configurations, which are easily perturbed by changes in the external elastic field. The results presented here showing stability of the subgrain structure towards stress relaxation contradict such an interpretation and limit the possible amount of instability.

Acknowledgments The authors wish to thank J. Almer, A. Mashyekhi, and S. D. Shastri for help during the experiments, and P. Nielsen, P. Olesen, and L. Lorentzen for sample preparation. This work was supported by the Danish National Research Foundation and the Danish Natural Science Research Council. Use of the Advanced Photon Source was supported by the U.S. Department of Energy, Office of Science, Office of Basic Energy Sciences, under Contract No. DE-AC02-06CH11357.

References

[1] U. Essmann, phys. stat. sol. **3**, 932 (1963).
[2] H. Mughrabi, Philos. Mag. **23**, 869 (1971).
[3] M. M. Myshlyaev, D. Caillard, and J. L. Martin, Scr. Metall. **12**, 157 (1978).
[4] M. Wilkens, phys. stat. sol. (a) **2**, 359 (1970).
[5] M. A. Krivoglaz, X-ray and Neutron Diffraction in Nonideal Crystals (Springer Verlag, Berlin, 1996).
[6] D. Breuer, P. Klimanek, and W. Pantleon, J. Appl. Crystallogr. **33**, 1284 (2000).
[7] R. Kuzel, Z. Kristallogr. **222**, 136 (2007).
[8] E. M. Lauridsen, S. Schmidt, R. M. Suter, and H. F. Poulsen, J. Appl. Crystallogr. **34**, 744 (2001).
[9] H. F. Poulsen, S. F. Nielsen, E. M. Lauridsen, S. Schmidt, R. M. Suter, U. Lienert, L. Margulies, T. Lorentzen, and D. Juul Jensen, J. Appl. Crystallogr. **34**, 751 (2001).
[10] B. C. Larson, W. Yang, G. E. Ice, J. D. Budai, and J. Z. Tischler, Nature **415**, 887 (2002).
[11] B. Jakobsen, H. F. Poulsen, U. Lienert, J. Almer, S. D. Shastri, H. O. Sørensen, C. Gundlach, and W. Pantleon, Science **312**, 889 (2006).
[12] B. Jakobsen, H. F. Poulsen, U. Lienert, and W. Pantleon, Acta Mater. **55**, 3421 (2007).
[13] H. Shankaranarayan and S. K. Varma, J. Mater. Sci. **30**, 3576 (1995).
[14] J. F. Wilson and N. K. Wilson, Trans. Soc. Rheol. **10**, 399 (1966).
[15] D. Caillard and J. L. Martin, Thermally Activated Mechanisms in Crystal Plasticity (Pergamon, Oxford, 2003).
[16] P. Feltham, J. Inst. Metall. **89**, 210 (1961).
[17] J. Kubat, Nature **205**, 378 (1965).
[18] G. Grimvall, J. Kubat, and M. Rigdahl, Mater. Sci. Eng. **27**, 45 (1977).

[19] O. Buck, phys. stat. sol. **3**, 1903 (1963).
[20] B. Jakobsen, H. F. Poulsen, U. Lienert, X. Huang, and W. Pantleon, Scr. Mater. **56**, 769 (2007).
[21] B. Jakobsen, U. Lienert, J. Almer, H. F. Poulsen, and W. Pantleon, Mater. Sci. Eng. A **483/484**, 641 (2008).
[22] R. W. Rohde and T. V. Nordstrom, Scr. Metall. **7**, 317 (1973).
[23] H. Mughrabi, T. Ungár, W. Kienle, and M. Wilkens, Philos. Mag. A **53**, 793 (1986).
[24] H. Mughrabi, Mater. Sci. Eng. **85**, 15 (1987).

